J. Am. Ceram. Soc., 97 [1] 251–257 (2014)
DOI: 10.1111/jace.12592

journal

Crack Growth Monitoring in Ceramic Matrix Composites by Combined Infrared Thermography and Acoustic Emission

Konstantinos G. Dassios,[‡,†] Evangelos Z. Kordatos,[‡] Dimitris G. Aggelis,[§] and Theodore E. Matikas[‡]

[‡]Department of Materials Science and Engineering, University of Ioannina, Ioannina 45110, Greece

[§]Department of Mechanics of Materials and Constructions, Vrije Universiteit Brussel, Pleinlaan 2 Brussels 1050, Belgium

The current study proposes a novel methodology for measuring crack growth in composite materials using combined infrared thermography (IRT) and acoustic emission (AE). The technique is tested across a SiC-fiber-reinforced ceramic matrix composite while no apparent factor is limiting its usage on composite materials of different nature as well. Compact tension specimens were loaded in tension with unloading/reloading loops and the thermally dissipated energy due to crack growth and other damage mechanisms was captured by IRT with a 100 Hz sampling rate. Crack growth was established by identifying the time instances where the maximum temperature, hence also damage, occurred and then quantifying, by means of control lines, the damage span within the thermograph corresponding to the specific instance. The high accuracy of the proposed technique was validated against optical measurements of crack length. The theoretical crack length predicted by the elastic compliance technique was found to overestimate the experimental findings by at least 25%. Knowledge of the critical level of damage accumulation for material structural health was made possible from AE descriptors such as activity during the unloading part of the cycles. In this study, AE was particularly successful in closely following the actual crack growth measured by IRT, an observation that brings out the potential of the technique for quantitative measurements.

I. Introduction

NATURALLY predestined for use in high-temperature applications, ceramic matrix composites (CMCs) can endow an aeronautical or astronautical structure with increased damage tolerance, fracture toughness, thrust-to-weight ratio, thermal shock, corrosion, and wear resistance over monolithic materials which are prone to catastrophic damage at such unavoidable defect sites as air cavities, pores, and microcracks in the otherwise continuous matrix medium.[1–3] Glass-ceramic matrix composites reinforced with continuous SiC fibers, in particular, have received a great deal of attention as they offer additional attractive properties such as high strength and stiffness, low density and chemical inertness at conventional and oxidative environments and over a wide range of temperatures.[4,5]

Due to the inherent anisotropy and inhomogeneity of CMCs, their quality assurance has—for many years—been a challenge.[6,7] The failure of the CMC-made thermal protection system (TPS) of space shuttle Columbia that lead to the disaster of February 1, 2003 intensified the need of reexamining available nondestructive evaluation (NDE) methods for (i) monitoring and evaluating component condition in real service time and (ii) detecting defects and cracks during the development stage of the materials that may result in early component failure. The National Aeronautics and Space Administration (NASA) routinely employs NDE techniques such as infrared thermography (IRT), ultrasound, acoustic emission (AE), advanced digital radiography, high-resolution computed tomography, and eddy current systems to detect defects in shuttle wings, airline rudders and tails, thruster chamber assemblies, combustion liners, and other composite components.[8–12] Recent advances in digital sensor technology and computer power have helped IRT imaging to reemerge as a most reliable damage inspection tool for advanced CMCs.[6] IRT is accurate, easy to implement, fast, noncontacting and only requires one-sided exposure. Among all available techniques, NASA relied exclusively on thermography for the initial inspection of TPS panels[9] of the (now decommissioned) orbiters. Astrium, the European Space Company, also employs thermography, X-rays, ultrasonics and AE,[13] as standard procedures for NDE of CMC components.

Although available NDE methodologies can successfully detect imperfections in advanced CMCs, assessment of the actual crack growth and its relation to the macroscopic mechanical behavior of such materials is still an open challenge. AE, IRT, digital image correlation, and transmitted light microscopy have been used to assess damage evolution,[14] fatigue life,[15] damage zone shape,[16] residual post-impact properties,[17] energy dissipation and degradation evolution[18] for polymer matrix composites or hybrid materials. A number of studies have also addressed NDE-based crack propagation measurements in material systems such as metals and alloys.[19–21] However, still no crack growth measurements are available for composites of ceramic, polymeric, or metallic matrices using NDE. IRT and AE were combined to measure thermal energy dissipation of some CMCs[22,23] as well as to monitor damage evolution in an alumina–boria–silica fiber-reinforced CMC under tension[24] and in a 2D carbon-fiber/SiC CMC under fatigue loading[25]; the results did not include crack growth data.

In the current work, a novel methodology is presented for monitoring and measuring crack propagation in CMCs by combined application, in real testing time, of IRT and AE. The methodology is tested on SiC-fiber-reinforced barium osumilite (barium–magnesium–aluminum–silicate, BMAS) glass-ceramic matrix composites loaded in cyclic tension with unloading–reloading loops under the compact tension (CT) specimen configuration. The technique can be applied to composite materials universally, as no apparent limitation to the nature of monitorable constituents is imposed.

E. Lara-Curzio—contributing editor

Manuscript No. 33093. Received April 25, 2013; approved July 29, 2013.
[†]Author to whom correspondence should be addressed. e-mail: kdassios@cc.uoi.gr

II. Experimental Procedure

The SiC/BMAS composite of this study was provided by AEA Technology (Harwell Ltd., Oxfordshire, UK) in 3-mm-thick cross-ply laminates. The reinforcing SiC fibers were grade "Tyranno" (UBE Industries Ltd., Ube, Japan) with nominal elastic modulus and strength values of 190 and 3.3 GPa, respectively, as reported by the manufacturer (reference gauge length not provided by manufacturer). The volume fraction of fibers in the composite was calculated as 0.55.[26] Composite processing involved eight main steps: (i) initial fiber heat treatment for removal of sizing, (ii) wetting of desized fibers in a slurry of the precursor glass frit, (iii) winding the fibers on a mandrel and allowing to dry for 20 min, (iv) preparation of prepreg sheets by cutting and arranging the fibers in layers, (v) stacking the sheets in $(0/90)_{4s}$ sequence, (vi) binder burn out, (vii) hot-pressing the sheets in a graphite die for 10 min at 1200°C, and (viii) crystallization by heat treatment at 1300°C. While the fibers were free of any surface coating prior to thermal curing, a chemical reaction between the SiC-fiber surface and the oxides of the matrix results is known to result in the formation of a carbon-rich interphase layer which provides a moderate fiber/matrix interfacial bond.[27] CT specimens with provision for load-line crack opening displacement (COD) measurement were prepared by abrasive water jet cutting according to ASTM E1820-01 specifications[28] and dimensions as per Fig. 1. The initial notch-to-width ratio of the CT specimens was 0.5.

Five CT samples of identical dimensions were tested under cyclic tension with unloading–reloading loops, at ambient temperature, on an Instron® 8800 servohydraulic frame (Instron, Norwood, MA) equipped with $a \pm 100$ kN load cell, hydraulic clamping grips, and ASTM E1820-01-compliant testing clevises.[28] Load-line COD was measured using an Instron® COD clip gauge with a gauge length of 10 mm and a maximum travel length of 4 mm. Testing was conducted under crosshead displacement control with a rate of 0.4 mm/min. The imposed unloading–reloading cycles were also based on crosshead displacement. The first unloading step commenced at 0.125 mm displacement and subsequent cycles occurred with a step of 0.075 mm. This cycling algorithm was chosen based on the tensile envelope curve of the material (established by pure tension testing) under the rationale that the material's total load-displacement behavior should accommodate at least 10 full unloading–reloading cycles, equally spaced within the maximum displacement span. All specimens were unloaded to complete relaxation; the reloading sequence was essentially triggered by the attainment of a zero load reading.

During testing, one side of the specimen—hereon, "front" side—was constantly monitored by an infrared thermographic camera (CEDIP, MIW) able to measure temperature variations due to the applied loading with a sensitivity of 20 mK. The camera features a cooled indium antimonide (InSb) detector (3–5 μm) and a focal plane array with pixel format of 320 (H) × 240 (V). Temperature was recorded with a sampling rate of 100 Hz. Aliasing was avoided by recording the baseline emissivity of the material prior to load application by capturing the IR fingerprint of the surface with the thermal camera. IRT images of temperature distributions recorded on the front side of composite specimens, termed "thermographs," were time stamped upon creation.

Acoustic Emission activity was also monitored on all specimens using two "Pico" miniature AE sensors (Physical Acoustics Corporation, Princeton, NJ) tape mounted on the "back" side of the specimen, at a separation of 40 mm. This manner of mounting allowed the front/IRT-monitored side of the specimen to be instrumentation-free. Acoustic coupling between the sensors and the specimen was provided by application of silicon grease. The broadband frequency response of the particular sensors, 50–800 kHz, enabled signal acquisition from a wide range of event sources. AE sampling was conducted on a PCI-2 board (Physical Acoustics Corporation, Princeton, NJ) with a sampling rate of 5 MHz, an amplification of 40 dB, and a threshold of 45 dB that enabled exclusion of ambient noise from the recorded signal. A 20 kHz–1.2 MHz band-pass filter was applied, while hardware parameters for AE acquisition were set as follows: peak definition time was set at 200 μs; hit definition time was 800 μs and hit lockout time was 1000 μs. Maximum duration was set at 1000 ms. The specific values were found to provide the best AE features for the material under investigation. They are, however, offered indicatively, as a number of external parameters may also apply in different setups which would make the AE trends look similar but actual values—such as, for example, AE hits—could be different. It must be noted that the small size of the specimens did not allow planar location of the AE sources. It was anticipated that such source location would not have provided essential additional information on the crack length as the specimen was monitored by IRT and could also be visually inspected.

Figure 2 provides graphical definitions of the most important AE parameters in a typical AE waveform. These parameters are: (i) the number of threshold crossings (counts), (ii) amplitude, A, which is the voltage of the highest cycle, and (iii) the rise time (RT) which is the delay between the first threshold crossing and the highest peak. The ratio of RT over A is the RA value which has proven very useful in assessing damage accumulation as well as in cracking mode characterization.[21,29] Average frequency is the number of counts to the duration, the latter is defined as the delay between the last and first threshold crossings of the waveform. Last, the energy (measured area under the rectified signal envelope, MARSE) is a dimensionless AE descriptor which has also proven useful in assessing damage.[30,31] In this study, all signals registered with zero energy were filtered out.

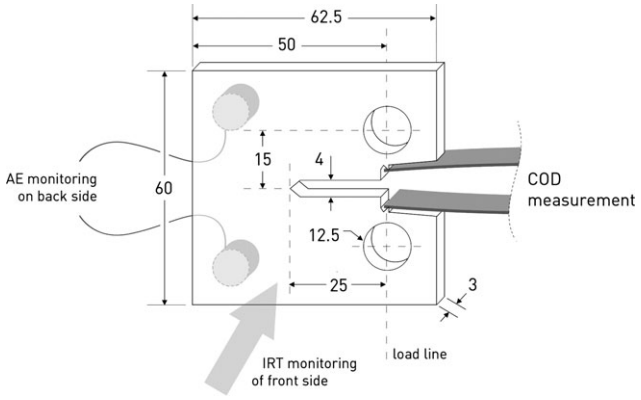

Fig. 1. CT specimen dimensions and arrangement of NDE instrumentation. Dimensions in mm.

III. Results and Discussion

Damage in brittle matrix composites is concentrated around propagating matrix cracks; their formation and propagation,

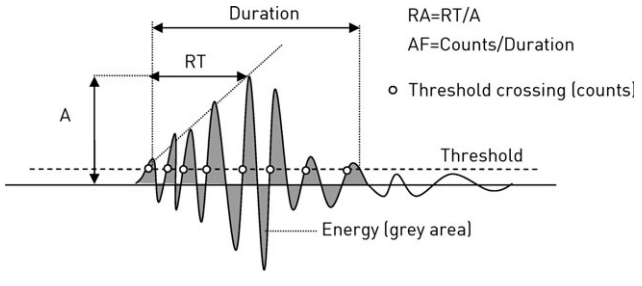

Fig. 2. Graphical definition of acoustic emission parameters.

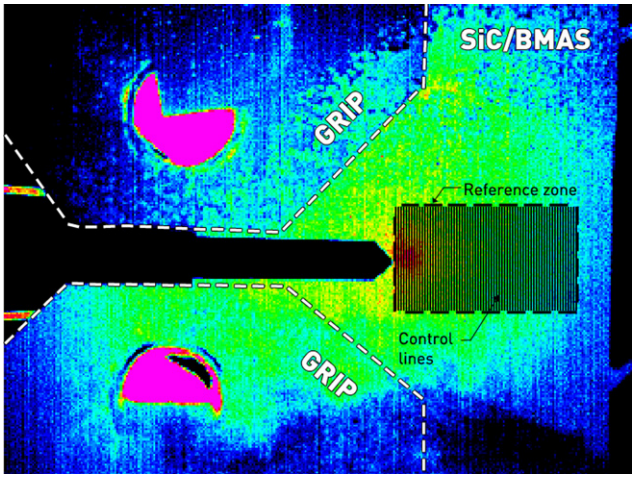

Fig. 3. Typical thermographic field-of-view during cyclic testing of SiC/BMAS composites with marked material and gripping system. The dashed rectangle marks the reference zone, i.e. the area considered for IRT data postprocessing, by division in subzones by means of equidistant control lines.

most frequently, appears first during testing as a result of the low strength and modulus of the continuous medium compared to the reinforcements. All major CMC damage mechanisms such as interfacial debonding, fiber sliding, bridging, and pull-out are, in one way or another, a result of crack formation and propagation.[32,33] Accepting that crack growth is the most severe CMC damage mechanism, hence also the energetically most prominent, a direct quantitative measure of the extent of cracking can be obtained by capturing the energy dissipated during CMC testing. Herein, measurement of crack growth in SiC/BMAS composites was made possible by adopting a novel methodology for analyzing the thermal energy dissipated by the material during testing and captured via IRT. This methodology is presented in the following.

Thermographs collected in real testing time were postprocessed with regard to temperature variations. Information from within a limited area in front of the notch root, where crack growth and damage were anticipated to concentrate, was considered. This area, termed the "reference zone", is shown schematically in Fig. 3. The zone dimensions were determined by circumscribing a rectangle to the maximum damage area span captured in the thermographs. For a typical test duration of 2000 s, 200 000 thermographs were postprocessed. Initially, for each experimental instance, the maximum temperature values within the reference zone, naturally relating to the maximum damage, were identified and plotted as function of their time stamp as shown in Fig. 4(a). In this plot, COD and cycle count are also included to facilitate perception of the instant loading level. The mechanical response of the CMC under cyclic loading is included in Fig. 4(b). It is observed that temperature variation exhibits periodical local maxima that are especially prominent after 1000 s of testing time, in contrast to the initial loading instances. Using Altair thermal image analysis software (FLIR Systems, Inc., Wilsonville, OR), the reference zone was divided into a large number of—equal in width—subzones by drawing successive neighboring vertical lines, called "control lines" (Fig. 3). The width of these lines was 0.226 mm, an experimentally fixed parameter essentially corresponding to the true size of 1 pixel in the thermal camera's native resolution for the specific filed-of-view. For a typical damage area span of 10 mm, corresponding to approximately 40% of the specimen's unnotched ligament, the reference zone contained 45 control lines. By knowing the exact time instance where these peak temperatures occur, from Fig. 4, and realizing that this peak value is the result of the crack path growing to a certain length, hence arriving at a certain control line, one can revisit the specific instance to identify the exact line, within the reference zone, where temperature maximizes. The established line count can then be straightforwardly converted to crack length using the aforementioned line width factor.

It is interesting to note that despite the sharp peaks near the maxima of the loading stages, temperature exhibits weak but consistently increasing trends during unloading which lead to local temperature peaks at the minimum of the cycles. Such behavior is seen more clearly from the eighth cycle on and is attributed to friction between closing crack flanks; the particular effect is discussed in the context of the instantaneous AE activity, in a following section.

IRT-measured crack length is plotted as a function of experimental time in Fig. 5 (hollow cycle symbols). It is observed that the initial five loading/unloading cycles do not induce crack formation or growth. A 0.45-mm-long crack is eventually formed at the sixth cycle, ~550 s into loading. In the subsequent 500 s, cycles 7 and 8, the crack does not appear to propagate further. Extensive—however stable—crack growth appears to commence after the eighth cycle, ~1100 s into loading. Within the subsequent 1000 s, or four cycles, crack length eventually reaches 9.3 mm, or ~37% of the specimen's unnotched ligament, before ultimate failure. Based on the above observations, crack growth behavior can be divided into three distinct regimes associated with different damage mechanisms: Regime 1 (R1), spanning testing times 0–550 s, or the first five unloading–reloading cycles, can be associated with null crack formation or growth; Regime 2 (R2), 550–1100 s (cycles 6, 7, and 8), is linked to

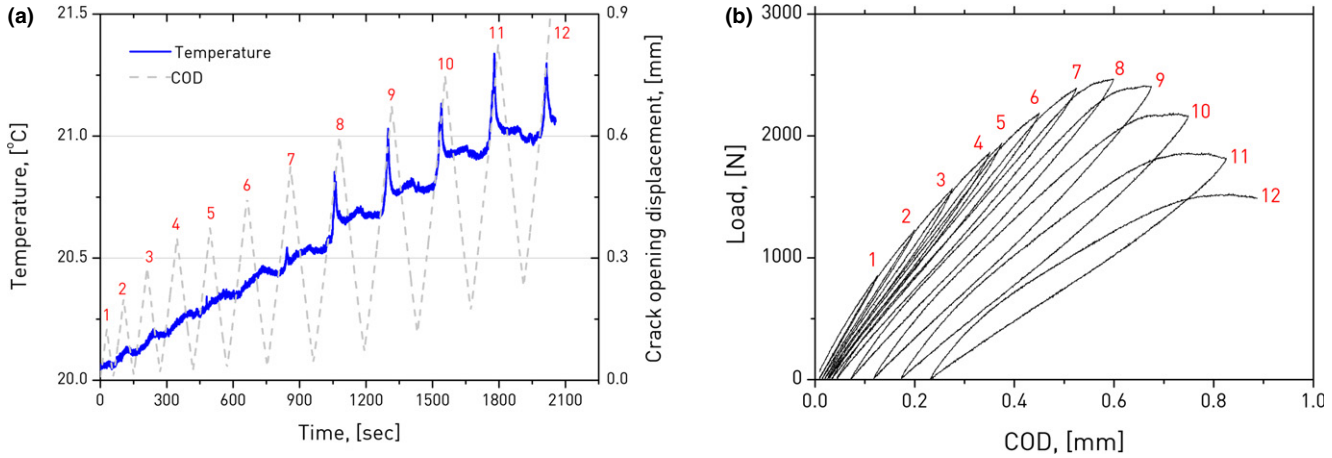

Fig. 4. (a) Typical profile of maximum temperature within the reference zone as a function of experimental time. (b) Typical load-crack opening displacement behavior of the material under cyclic loading. Red numerals denote cycle count.

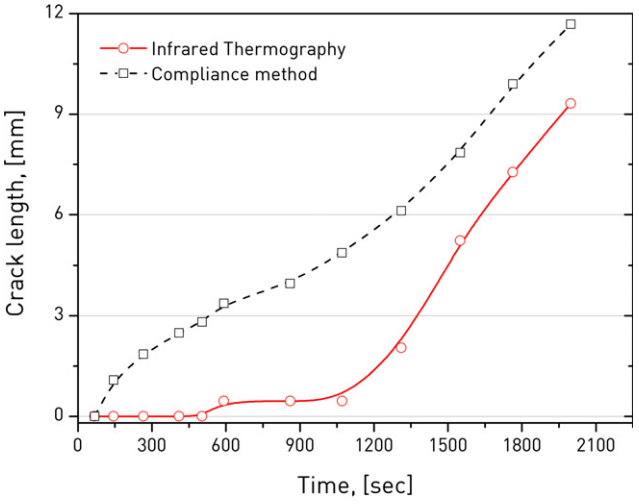

Fig. 5. Comparison of IRT-measured and theoretically predicted crack growth. Lines represent cubic spline regressions to the data.

minimal matrix cracking and interfacial damage phenomena; and Regime 3 (R3), 1100 s up to fracture (last four cycles), is dominated by extensive matrix cracking, fiber bridging, failure, and pull-out. It must be noted that, for the particular specimen configuration, crack growth can only span a fraction of the unnotched ligament of the material as a result of the compressive forces that develop at the specimen's backface. Plotted alongside the experimentally measured (IRT) crack growth in Fig. 5 are the model predictions based on the conventional elastic compliance technique.[28] A wide discrepancy between experimental and model values is observed, especially within the initial nine cycles where crack growth is not significant. We believe that this discrepancy is due to the shortcoming of the analytical method to approach compliance changes independently of crack growth. Contrary to the model approach, where compliance drops are considered only in the presence of crack growth, in a CMC, such decreases can also be promoted by independent mechanisms such as high stress concentration at the crack tip. Moreover, in view of the brittle nature of the glass-ceramic matrix, crack growth is not expected to follow the highly stable, almost linear, trend predicted by theory. Under the same rationale, within the last three unloading/reloading stages related to stable crack growth, the experimental values appear to follow the model-predicted trend, albeit an overestimation in actual crack length values of 25%.

The accuracy of the IRT technique was validated against direct optical observations of crack length on failed CT specimens, performed postmortem using a Leica MZ7.5 stereoscope (Leica Microsystems, Wetzlar, Germany). As shown in Fig. 6, crack growth reaches 9.2 mm for the CT specimen with an IRT-established maximum crack length of 9.3 mm (Fig. 5). The exceptionally favorable comparison of the two values confirms the validity and accuracy of the thermographic technique proposed herein for crack measurement.

Figure 7 represents typical thermographs collected at indicative successive stages of crack growth. Warmer colors correspond to higher amounts of thermally dissipated energy, hence represent areas of higher damage accumulation as opposed to colder colors. Violet color, corresponding to the maximum temperature, is attributed to crack growth. The onset of cracking is barely seen in Fig 6(a), 1100 s into testing. As the crack propagates, the damage zone expands radially due to stress transfer from the high stress area to the surrounding material but also due to the unfolding of complementary damage mechanisms such as interfacial damage, fiber sliding along the debonded interface, fiber bridging, and pull-out.[34] Figure 7(e), collected just before composite failure, represents the maximum damage span on the specimen. Using image analysis, the contours to the maximum temperature zones found at the crack tip (violet color) can be reconstructed as shown in Fig. 7(f). In this manner, the shape and size of the damage zone and its evolution with time during composite fracture can be visualized.

Acoustic emission results provided valuable feedback on the role, magnitude, and evolution of damage during testing. Figure 8(a) represents the time history of the cumulative received AE energy, along with load-line COD. It is observed that the rate of accumulating energy is increasing as the strain is reaching the peak of each cycle, an observation indicating increased damage accumulation within this specific regime. During the descending part of each cycle, the activity is certainly lower but not negligible especially for the last cycles of higher maximum strain. The sharp increase in the AE line observed at cycle 8, indicated with an arrow, compares favorably with the earlier-discussed increase in crack length observed via IRT at the same instance (Fig. 5). Acoustic emission was also capable of capturing the relation between crack growth and elastic energy: longer crack growths resulted in higher amounts of released elastic energy. Figure 8(b) shows the RA values for the entire population of AE signals. It is noted that RA increases with strain within each cycle, while low RA values are seen at the descending part of load-line COD. Analogous behavior has been documented in the past.[26] One important observation is that, within the last unloading/reloading cycles, noticeable AE activity is recorded also at the descending part of the cycles, as indicated by the elliptical marks in Fig. 8(b). While the

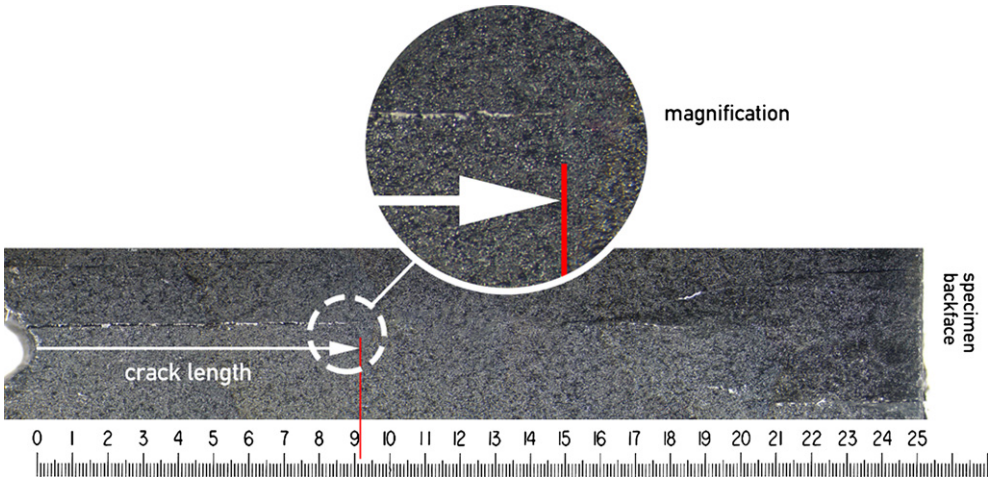

Fig. 6. Optical stereoscope image of the failed ligament of a CT specimen. Note notch root on the left side and compressive damage on the rear and backface of the specimen. Scale bar in mm.

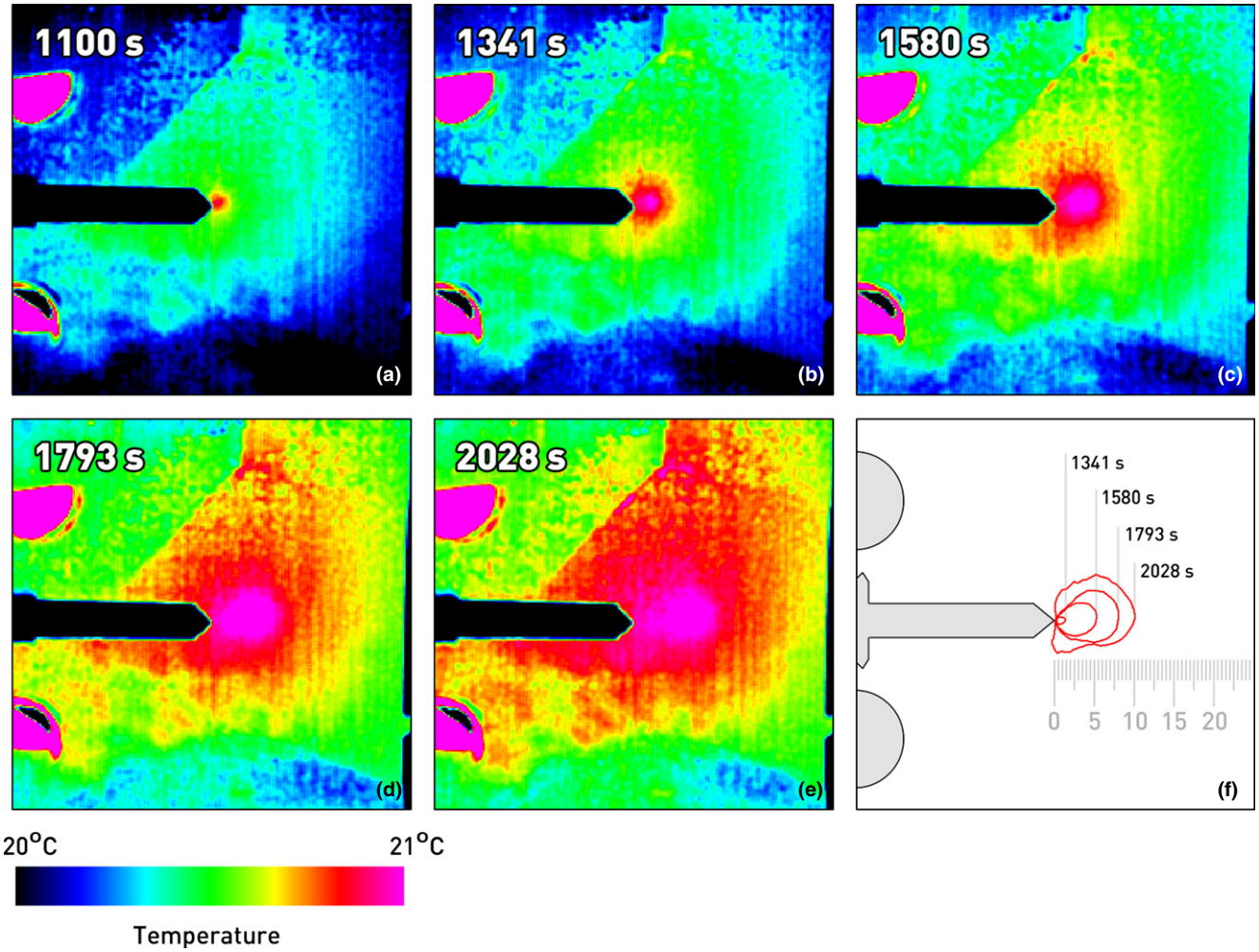

Fig. 7. (a)–(e) Indicative thermographs showing crack growth and extent of damage during composite fracture. (f) Contour plots (red lines) of maximum damage zones at crack tip, Scale bar in mm.

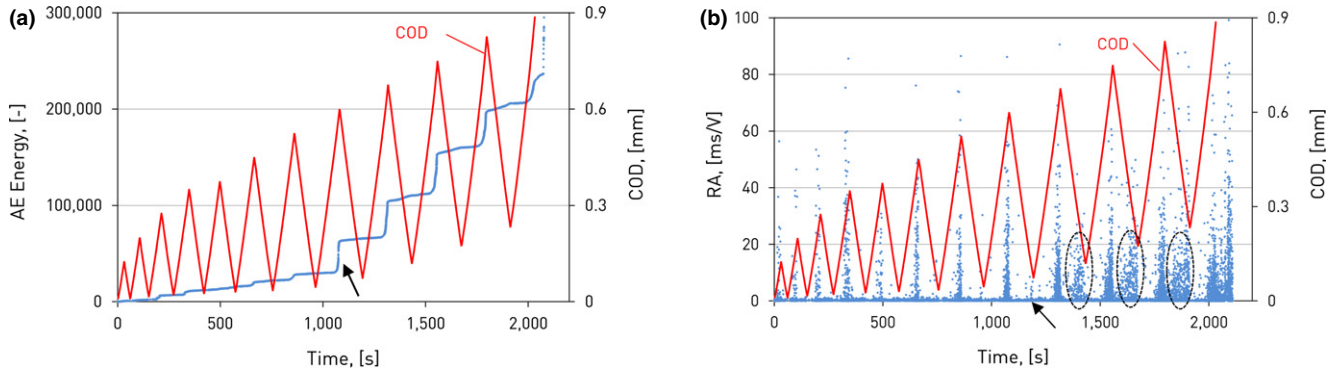

Fig. 8. (a) Cumulative acoustic emission (AE) energy history and (b) RA of entire AE signal population.

effect is noted clearly from the ninth cycle on, initial indications are present also in the unloading part of the eighth cycle, as denoted by the arrow in Fig. 8(b). This kind of significant activity during unloading is indicative of extensive damage accumulation in the material.[30] It is worth mentioning that AE during unloading does not necessarily imply that new damage sources emerge. Recording of large amounts of AE during unloading of a material/structure is a phenomenon associated with high levels of damage already accumulated during loading and is indicative of structural integrity.[29] The use of AE information during unloading is included in recommendations for practical use and is termed "secondary AE".[29] In this case, AE is attributed to friction between matrix crack faces or debonded fiber-matrix interfaces which did not occur at low load levels where cracking and debonding are absent.

Given the non-monotonic nature of the testing protocol (unloading–reloading), an investigation of the existence of possible "Kaiser effects"[29] appears particularly interesting. AE recordings after the previous maximum load/strain has been surpassed are signs of good structural health; when severe flaws are present AE activity starts earlier than the previous maximum. This phenomenon is quantified by the "felicity ratio," which is the ratio of the load value at the

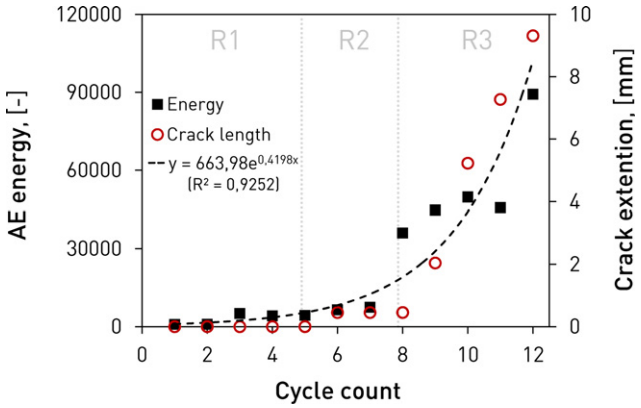

Fig. 9. MARSE AE energy and crack extension as a function of cycle count.

onset of AE over the previous maximum load value. In the present case, AE appears intensified before displacement reaches the value corresponding to the previous maximum; this effect is particularly evident during the last cycles and is indicative of severe damage accumulation within these cycles. However, the rich activity during unloading does not allow the determination of an "onset" of AE within each cycle; AE is almost continuously recorded. Therefore, felicity ratio analysis was not considered for the particular datasets.

The merged plot of AE energy and IRT-measured crack extension as functions of cycle count is presented in Fig. 9. In this figure, solid square symbols represent AE energy, the dashed line is the exponential best-fit function to the AE data and hollow cycles are the IRT-measured crack lengths. It is observed that AE energy follows the triple regime trend discussed earlier in the crack extension versus time behavior (Fig. 5). This is most prominent in R3, after the eighth cycle and 1100 s of testing, where the emitted energy is more than five times higher than previous cycles. AE energy in R1 is almost null within the first two cycles and increases slightly in the third cycle. The energy remains essentially constant throughout the fourth and fifth cycle and increases slightly again in cycles 6 and 7 of R2, where material damage is expressed as limited matrix cracking and interfacial damage.

Normalized cumulative AE activity recorded within each unloading/reloading cycle is plotted in Fig. 10(a) alongside the activity upon unloading which is considered separately due to the consistent increase discussed in the previous paragraph. The total number of hits appears to closely follow a steep exponential increase as a function of cycle count. AE activity on unloading, represented with dashed red line in Fig. 10(a), follows an increasing cubic spline trend with a prominent jump consistently appearing after the eighth step. This observation independently validates the previous claim of a rapid material deterioration between the eighth and ninth cycle. Figure 10(b) shows the relation between AE activity during loading and unloading and crack growth measured by IRT, for each cycle. A very good correlation is noted ($R^2 > 0.95$) which suggests that AE activity can act as a powerful descriptor for passive monitoring of the crack growth. The observed natural logarithmic type of correlation is linked to the existence of one single crack. Then, the whole AE energy received by the sensors is associated with the propagation of the specific crack. On the other hand, crack length depends on the amount of fracture energy released as elastic waves by the creation of crack surfaces. AE energy is part of this fracture energy. Therefore, the length of the crack and AE activity are linked to the same process which allows the observed correlations. Hence, the form of correlation between AE parameters and the crack length occurs as a result of the consumption of the total amount of fracture energy (part of which was recorded as AE) required to propagate the single crack. Similar correlations between energy and crack length have been documented in metal specimens under cyclic loading.[31,35] As observed in Fig. 10(b), AE activity during unloading is also well-correlated with crack length. This happens because, as crack length increases with cycle count, the surface span on friction expands, hence AE emissions increase during unloading. It is interesting to note that during the last cycles, AE activity upon unloading is higher than the loading stage due to extensive friction between the long crack sides. For the final stages, although the number of emissions during unloading is higher than during loading, these emissions are energetically inferior. In fact, the total accumulated energy recorded during the loading stages is five times higher than the energy at unloading. Therefore, most of the fracture energy is emitted at severe damage incidents during loading, naturally relating to crack propagation, which also results in the temperature peaks documented in Fig. 4(a). Friction between the crack flanks during unloading triggers certain amounts of AE activity of lower energy. Analogously, small temperature peaks registered at the end of the unloading stages, from the eighth cycle on, are attributed to friction-related heat dissipation.

The exact numerical form of the fitting equations of Fig. 10 is connected to the specific monitoring setup including specimen geometry, type of material, sensor location and type and loading protocol. Accepting that AE activity occurs as a direct result of fracture and other damage mechanisms, similar trends should be expected in a modified setup. However, the exact values of the fitting functions' parameters should be investigated for each specific setup and loading protocol because the selection of the number of cycles and increase of maximum load between successive cycles will certainly affect the distribution of the AE energy within the duration of the experiment. In many cases, due to the large number of active sources, AE conclusions are qualitative and used for compari-

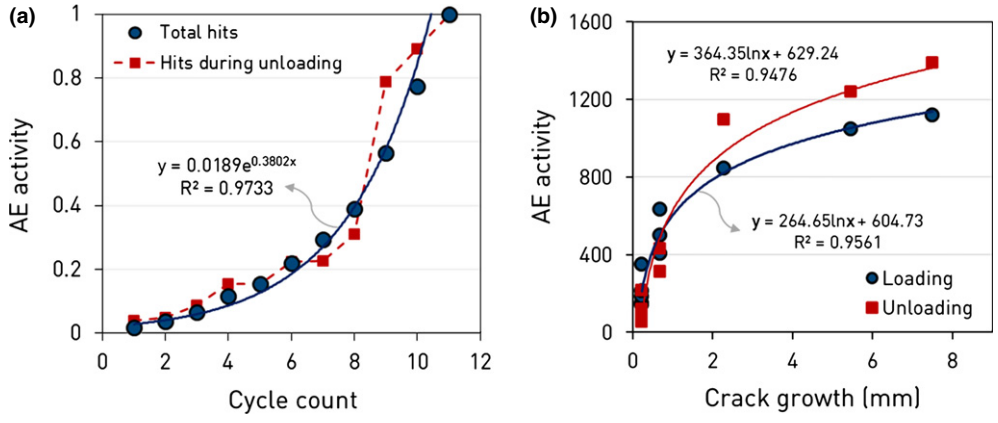

Fig. 10. (a) AE activity and (b) correlation between AE activity and crack growth for successive loading steps.

son purposes between different types of materials or loading cases. The good correlation of AE parameters with crack length, due to the existence of a single crack in this case, aims to demonstrate the potential of AE for quantitative damage characterization. This does not imply that the same exact line would fit results from other types of experiments. Conducting experiments on other specimen geometries in order to investigate the behavior of the fitting parameters and examine whether a master curve can be established, actually emerges as a challenging task. On the other hand, having established the fundamentals for the application of the proposed method, testing its efficiency under more complex loading scenarios, such as high-cycle fatigue, appears interesting.

IV. Conclusions

A combination of real-time IRT and AE techniques was used to measure and validate crack growth in SiC/BMAS glass-ceramic matrix composites loaded in tension with unloading–reloading loops under the CT specimen configuration. The novel aspects of the proposed method include: (i) real-time crack growth measurements in composites using combined NDE techniques, (ii) potential for application on composite materials of any nature, (iii) exceptionally good resolution and accuracy of measured crack length, and (iv) potential as a benchmarking tool for available crack growth prediction models. The energy dissipated due to crack growth during testing was quantified by postprocessing of thermographic information collected with a 100 Hz sampling rate within a reference zone in front of the crack tip divided into 0.226-mm-wide subzones. Crack length for each cycle was established by identification of the time stamp of peaks in the plot of maximum temperature versus time and subsequent detection of the subzone of highest damage span in the thermograph corresponding to the specific instance. Crack growth was significantly overestimated by the conventional elastic compliance technique especially during the initial loading stages where changes in composite compliance do not essentially stem from matrix cracking. The efficiency of the proposed thermographic technique was validated within exceptionally good accuracy against direct observations of crack length on failed specimens. Image analysis was used to visualize the variation in shape and size of the damage zone during composite fracture. AE descriptors such as total activity, activity during unloading, and waveform features like RA proved valuable in monitoring material changes related to crack growth and in enabling knowledge of the level of critical damage accumulation that can compromise the material's structural health.

References

[1]H. Mei, L. F. Cheng, X. G. Luan, L. T. Zhang, Y. D. Xu, and D. Wang, "Simulated Environments Testing System for Advanced Ceramic Matrix Composites," *Int. J. Appl. Ceram. Technol.*, **3**, 252–7 (2006).

[2]R. Naslain, "Design, Preparation and Properties of Non-Oxide CMCs for Application in Engines and Nuclear Reactors: An Overview," *Compos. Sci. Technol.*, **64**, 155–70 (2004).

[3]S. Schmidt, S. Beyer, H. Immich, H. Knabe, R. Meistring, and A. Gessler, "Ceramic Matrix Composites: A Challenge in Space-Propulsion Technology Applications," *Int. J. Appl. Ceram. Technol.*, **2**, 85–96 (2005).

[4]K. M. Prewo, J. J. Brennan, and G. K. Layden, "Fiber Reinforced Glasses and Glass-Ceramics for High-Performance Applications," *Am. Ceram. Soc. Bull.*, **65**, 305–13 (1986).

[5]J. J. Brennan and K. M. Prewo, "Silicon-Carbide Fiber Reinforced Glass-Ceramic Matrix Composites Exhibiting High-Strength and Toughness," *J. Mater. Sci.*, **17**, 2371–83 (1982).

[6]H. Mei, "Current Development in Non-Destructive Testing and Damage Evaluation for Ceramic Matrix Composites," *Adv. Appl. Ceram.*, **108**, 84–91 (2009).

[7]S. Schmidt, S. Beyer, H. Knabe, H. Immich, R. Meistring, and A. Gessler, "Advanced Ceramic Matrix Composite Materials for Current and Future Propulsion Technology Applications," *Acta Astronaut.*, **55**, 409–20 (2004).

[8]J. G. Sun, M. J. Verrilli, R. Stephan, T. R. Barnett, and G. Ojard, "Nondestructive Evaluation of Ceramic Matrix Composite Combustor Components"; NASA/TM-2003-212014, April, 2003.

[9]E. I. Madaras, W. P. Winfree, W. H. Prosser, R. A. Wincheski, and K. E. Cramer, "Nondestructive Evaluation for the Space Shuttle's Wing Leading Edge"; AIAA 2005-3630, July, 2005.

[10]W. P. Winfree, E. I. Madaras, K. E. Cramer, P. A. Howell, K. L. Hodges, J. P. Seebo, and J. L. Grainger. "NASA Langley Inspection of Rudder and Composite Tail of American Airlines Flight 587"; AIAA 2005–2253, April, 2005.

[11]H. Mei, Y. D. Xu, L. F. Cheng, and L. T. Zhang, "Nondestructive Evaluation and Mechanical Characterization of a Defect-Embedded Ceramic Matrix Composite Laminate," *Int. J. Appl. Ceram. Technol.*, **4**, 378–86 (2007).

[12]J. G. Sun, C. M. Deemer, W. A. Ellingson, and J. Wheeler, "NDT Technologies for Ceramic Matrix Composites: Oxide and Nonoxide," *Mater. Eval.*, **64**, 52–60 (2006).

[13]F. Levallois, A. Sobeczko, A. Proust, D. Marlot, and J.-C. Lenain, "Non-Destructive Testing of GAIA Frame by Means of Acoustic Emission Monitoring During Launch Simulation Tests"; 30th European Conference on Acoustic Emission Testing & 7th International Conference on Acoustic Emission, University of Granada, Spain, 2012.

[14]J. Cuadra, P. A. Vanniamparambil, K. Hazeli, I. Bartoli, and A. Kontsos, "Damage Quantification in Polymer Composites Using a Hybrid NDT Approach," *Compos. Sci. Technol.*, **83**, 11–21 (2013).

[15]A. N. Kahirdeh, M. Naderi, and M. M. Khonsari, "On the Role of Cooling on Fatigue Failure of a Woven Glass/Epoxy Laminate," *J. Compos. Mater.*, **47**, 1803–15 (2012).

[16]J. Kargerkocsis and Z. Fejeskozma, "Failure Mode and Damage Zone Development in a GMT-PP by Acoustic-Emission and Thermography," *J. Reinf. Plast. Compos.*, **13**, 768–92 (1994).

[17]I. M. De Rosa, C. Santulli, F. Sarasini, and M. Valente, "Post-Impact Damage Characterization of Hybrid Configurations of Jute/Glass Polyester Laminates Using Acoustic Emission and IR Thermography," *Compos. Sci. Technol.*, **69**, 1142–50 (2009).

[18]M. Naderi, A. Kahirdeh, and M. M. Khonsari, "Dissipated Thermal Energy and Damage Evolution of Glass/Epoxy Using Infrared Thermography and Acoustic Emission," *Compos. B Eng.*, **43**, 1613–20 (2012).

[19]B. Yang, G. Wang, W. H. Peter, P. K. Liaw, R. A. Buchanan, D. E. Fielden, Y. Yokoyama, J. Y. Huang, R. C. Kuo, J. G. Huang, and D. L. Klarstrom "Thermal-Imaging Technologies for Detecting Damage during High-Cycle Fatigue," *Metall. Mater. Trans. A*, **35A**, 15–23 (2004).

[20]D. A. Aouit and A. Ouahabi, "Monitoring Crack Growth Using Thermography," *C.R. Mec.*, **336**, 677–83 (2008).

[21]E. Z. Kordatos, D. G. Aggelis, and T. E. Matikas, "Monitoring Mechanical Damage in Structural Materials Using Complimentary NDE Techniques Based on Thermography and Acoustic Emission," *Compos. B Eng.*, **43** [6] 2676–86, 2012.

[22]B. Li, X. Tong, Z. Feng, and L. Yao, "Infrared Thermography and Acoustic Emission in 2D Plain Woven C/Sic Composites under Tensile-Tensile Fatigue Loading," *Adv. Mater. Res.*, **118–120**, 251–5 (2010).

[23]J. Kim, "Analysis of Heat Generation During Fracture in Ceramic Matrix Composites," *Key Eng. Mater.*, **385–387**, 689–92 (2008).

[24]J. Kim and P. K. Liaw, "Monitoring Tensile Damage Evolution in Nextel 312/Blackglas (TM) Composites," *Mater. Sci. Eng., A*, **409**, 302–8 (2005).

[25]C. D. Liu, L. F. Cheng, X. G. Luan, B. Li, and J. Zhou, "Damage Evolution and Real-Time Non-Destructive Evaluation of 2D Carbon-Fiber/SiC-Matrix Composites under Fatigue Loading," *Mater. Lett.*, **62**, 3922–4 (2008).

[26]K. G. Dassios, D. G. Aggelis, E. Z. Kordatos, and T. E. Matikas, "Cyclic Loading of a SiC-Fiber Reinforced Ceramic Matrix Composite Reveals Damage Mechanisms and Thermal Residual Stress State," *Compos. A Appl. Sci. Manuf.*, **44**, 105–13 (2013).

[27]R. F. Cooper and K. Chyung, "Structure and Chemistry of Fiber Matrix Interfaces in Silicon–Carbide Fiber-Reinforced Glass Ceramic Composites – an Electron-Microscopy Study," *J. Mater. Sci.*, **22**, 3148–60 (1987).

[28]ASTM Standard E 1820, 2001, "Standard Test Method for Measurement of Fracture Toughness"; ASTM International, West Conshohocken, PA, 2001. DOI: 10.1520/E1820-01, www.astm.org.

[29]M. Ohtsu, T. Shiotani, M. Shigeishi, T. Kamada, S. Yuyama, T. Watanabe, T. Suzuki, J. G. M. Van Mier, T. Vogel, C. Grosse, R. Helmerich, M. C. Forde, A. Moczko, D. Breysse, S. A. Ivanovich, A. Sajna, D. Aggelis, and G. Lacidogna "Recommendation of RILEM TC 212-ACD: Acoustic Emission and Related NDE Techniques for Crack Detection and Damage Evaluation in Concrete Test Method for Damage Qualification of Reinforced Concrete Beams by Acoustic Emission," *Mater. Struct.*, **43**, 1183–6 (2010).

[30]C. U. Grosse, *Acoustic Emission Testing: Basics for Research - Applications in Civil Engineering*. Springer, New York, 2008.

[31]T. M. Roberts and M. Talebzadeh, "Acoustic Emission Monitoring of Fatigue Crack Propagation," *J. Constr. Steel Res.*, **59**, 695–712 (2003).

[32]M. D. Thouless and A. G. Evans, "Effects of Pull-Out on the Mechanical-Properties of Ceramic-Matrix Composites," *Acta Metall. Mater.*, **36**, 517–22 (1988).

[33]K. G. Dassios, V. Kostopoulos, and M. Steen, "Intrinsic Parameters in the Fracture of Carbon/Carbon Composites," *Compos. Sci. Technol.*, **65**, 883–97 (2005).

[34]K. G. Dassios, "A Review of the Pull-Out Mechanism in the Fracture of Brittle-Matrix Fibre-Reinforced Cowosites," *Adv. Compos. Lett.*, **16**, 17–24 (2007).

[35]B. A. Zarate, J. M. Caicedo, J. G. Yu, and P. Ziehl, "Probabilistic Prognosis of Fatigue Crack Growth Using Acoustic Emission Data," *J. Eng. Mech. - ASCE*, **138**, 1101–11 (2012). □